Article

Not peer-reviewed version

Photocatalytic Degradation, Anticancer, and Antibacterial Studies of Lysinibacillus sphaericus Biosynthesized Semiconductor and Hybrid Metal/Semiconductor Nanoparticles

Kannan Badri Narayanan *, Rakesh Bhaskar , Yong Joo Seok , Sung Soo Han

Posted Date: 3 July 2023

doi: 10.20944/preprints202307.0022.v1

Keywords: Silver/zinc oxide nanoparticles; Semiconductor; Microbial biosynthesis; Photodegradation; Cytotoxicity; Antibacterial

Article

Photocatalytic Degradation, Anticancer, and Antibacterial Studies of *Lysinibacillus sphaericus* Biosynthesized Semiconductor and Hybrid Metal/Semiconductor Nanoparticles

Kannan Badri Narayanan [a,b,*], Rakesh Bhaskar, Yong Joo Seok and Sung Soo Han [a,b,*]

[a] School of Chemical Engineering, Yeungnam University, 280 Daehak-Ro, Gyeongsan, Gyeongbuk 38541, South Korea
[b] Research Institute of Cell Culture, Yeungnam University, 280 Daehak-Ro, Gyeongsan, Gyeongbuk 38541, South Korea
* Correspondence: okbadri@gmail.com or okbadri@yu.ac.kr (K.B.N.); sshan@yu.ac.kr (S.S.H.)

Abstract: The biological synthesis of nanoparticles has been emerging as an environmentally benign and eco-friendly method owing to its cost-effectiveness and high efficiency. Recently, the biological synthesis of semiconductor and metal-doped semiconductor nanoparticles with enhanced photocatalytic degradation efficiency and anticancer and antibacterial properties have gained tremendous attention. In pursuit of this purpose, for the first time, we biosynthesized zinc oxide (ZnO) and silver/ZnO nanocomposites (NCs) as semiconductor and metal-doped semiconductor nanoparticles, respectively, using the cell-free filtrate (CFF) of *Lysinibacillus sphaericus* bacterium. The biosynthesized ZnO and Ag/ZnO were characterized by various techniques such as ultraviolet-visible spectroscopy, X-ray diffraction, Fourier-transform Infrared spectroscopy, Field-emission scanning electron microscopy, transmission electron microscopy, and photoluminescence spectroscopy. The photocatalytic degradation potential of these semiconductor/metal-semiconductor nanoparticles was evaluated against the degradation of azo dye methylene blue (MB) under simulated solar irradiation. Ag/ZnO showed 90.7 ± 0.91% photocatalytic degradation of MB, compared to 50.7 ± 0.53% by ZnO in 120 min. The cytotoxicity of ZnO and Ag/ZnO on human cervical HeLa cancer cells was determined using an MTT assay. Both nanomaterials exhibited cytotoxicity in a concentration-dependent and time-dependent manner on HeLa cells. The antibacterial activity was also determined against Gram-negative (*Escherichia coli*) and Gram-positive (*Staphylococcus aureus*). Compared to ZnO, Ag/ZnO NPs showed higher antibacterial activity. Hence, the biosynthesis of semiconductor nanoparticles could be a promising strategy for developing hybrid metal/semiconductor nanomaterials for different biomedical and environmental applications.

Keywords: Silver/zinc oxide nanoparticles; Semiconductor; Microbial biosynthesis; Photodegradation; Cytotoxicity; Antibacterial

1. Introduction

The industrial revolution in the current world has produced numerous associated environmental pollutants, which is a great concern for humankind. In particular, textile and dyeing industries and other industries where several organic dyes are used and the release of dye-contaminated industrial effluents as refractory pollutants contaminants nearby waterbodies and threatens humans and aquatic lives [1]. Textile dye effluent is one of the major pollution problems in the world. These dye-contaminated effluents pollute soil, surface water, and groundwater [2]. Until the early 19th century, natural dyes were used for coloring textiles and other decorations. In 1856, William H. Perkin was the first to synthesize the synthetic organic dye "mauveine" while attempting to synthesize the antimalarial drug quinine [3,4]. By far, several dyes are produced through azo coupling and produced in several million tons every year globally. These dye effluents can hinder the photosynthetic activity of aquatic plants, algae, and phytoplanktons and reduce oxygen

 doi:10.20944/preprints202307.0022.v1

production, accelerating the impacts of climate change effects. It is estimated that 50-80% of oxygen production comes from the photosynthetic activity of phytoplanktons [5]. These synthetic refractory dyes must be degraded to protect the ecosystem from their toxic effects.

Generally, various physical and chemical methods such as adsorption, precipitation, coagulation-flocculation, electrolysis, ultrasound, advanced oxidation processes (AOPs), photocatalysis, reduction, electrochemical treatment, Fenton process, and ion exchange are used for the removal and degradation of dyes from industrial effluents [6,7]. Nevertheless, these methodologies are expensive and require sophisticated instruments. Moreover, there are also biological methods using microbes such as *Brevibacillus* sps., *Brachymonas* sps., *Bacillus* sps., *Pseudomonas* sps., *Acinetobacter* sps. *Fusarium* sps. *Trichoderma* sps. and mixed cultures and genetically engineered microorganisms for the bioremediation of dyes from industrial effluents [8–10]. Although these biological methods provide cost-effective and eco-friendly nature in the degradation of dyes, they are time-consuming. In this scenario, nanotechnology-driven methodologies can offer efficient solutions to managing dye-contaminated industrial effluents. The efficiency of nanomaterials is greatly based on the type of metal or metal oxide nanoparticles, smaller dimension, and their large surface-to-volume ratio [11]. The synthesis of these nanoparticles with unique physicochemical and optical properties can also fall under the physical, chemical, and biological categories. Again, the biological synthesis of nanoparticles is preferred due to the adherence to their green principles over other synthetic routes [12]. Thus, microbial-mediated syntheses of nanoparticles are advantageous.

Metal/metal oxide nanoparticles composed of gold, silver, zinc, copper, palladium, platinum, or ruthenium are commonly used photocatalysts for environmental remediation applications. Among the various photocatalysts, zinc oxide (ZnO) is an excellent semiconductor photocatalyst. However, the band gap energy of 3.37 eV limits the most efficient photocatalytic degradation of dyes by ZnO under ultraviolet (UV) light and is less efficient under visible wavelength [13]. Many attempts, such as the increasing of specific surface area and refining the grain size, have been reported to improve the photocatalytic performance of ZnO [13–15]. Currently, element doping and recombination with metals or semiconductors are commonly used to improve the photoresponse range of ZnO as photocatalysts. Kareem et al. [16] demonstrated the synthesis of silver-doped ZnO nanoparticles and their enhanced photocatalytic ability of ZnO NPs towards methylene blue (MB) degradation than undoped ZnO NPs. The incorporation of Ag-doped ZnO nanorod through graphite hybridization (ZnO-Ag-Gp) exhibited degradation of pharmaceutical pollutant ciprofloxacin [17]. These semiconductor and hybrid metal/semiconductor nanoparticles also exhibit high cytotoxicity against cancer cells and possess strong antimicrobial activity [18]. In our study, we demonstrated, for the first time, the biosynthesis and characterization of zinc oxide (ZnO) and silver/ZnO (Ag/ZnO) nanoparticles using the cell-free filtrate (CFF) of *L. sphaericus*. These nanoparticles were evaluated for their photodegradation efficiency of an azo dye, *in vitro* cytotoxicity efficiency against HeLa cancer cells and antibacterial properties against Gram-positive and -negative bacteria.

2. Materials

Zinc nitrate hexahydrate ($Zn(NO_3)_2{\cdot}6H_2O$) (extra pure grade), dipotassium phosphate (K_2HPO_4), and methylene blue (MB) were obtained from Duksan Pure Chemicals Co., Ltd (Ansan-si, South Korea). *Lysinibacillus sphaericus* (ATCC 14577) was purchased from American Type Culture Collection (VA, USA). *Escherichia coli* (KCTC 2571) and *Staphylococcus aureus* (KCTC 3881) were obtained from the Korean Collection for Type Cultures (Jeongeup, South Korea). Malt extract, tryptone peptone, yeast extract, soytone, and agar were purchased from Difco™ (Detroit, MI, USA). MTT (3-(4,5-dimethylthiazol-2-yl)-2,5-diphenyltetrazolium bromide) and silver nitrate was purchased from Sigma-Aldrich (USA). Human cervical cancer cell line (HeLa) (CCL-2) was purchased from the American Type Culture Collection (ATCC) (Manassas, VA, USA). Eagle's minimum essential medium (EMEM), fetal bovine serum (FBS), penicillin/streptomycin, 0.25% trypsin-EDTA, and 1% penicillin/streptomycin were purchased from Gibco™ (Thermo Fisher Scientific, USA). Deionized water collected from the Milli-Q® Direct water purification system (Merck Millipore, Darmstadt, Germany) was used for experiments.

 doi:10.20944/preprints202307.0022.v1

2.1. Culturing of Lysinibacillus Sphaericus Bacterium

Bacterium *Lysinibacillus sphaericus* was cultured on tryptic soy agar (TSA) and the purified bacterium was grown on TS broth (containing 17 g/L tryptone peptone, 3 g/L soytone, 5 g/L NaCl, 2.5 g/L glucose, 2.5 g/L K_2HPO_4) at 30 °C for 16 h on a rotary shaker [19]. 1% (v/v) of this culture was used as an inoculum to culture 100 mL TS medium in a 250 mL Erlenmeyer flask for 16 h. Later, the culture was centrifuged to pellet bacterial biomass at 4,000 rpm for 20 min at 4 °C, and the supernatant was filtered through a nylon filter membrane with 0.45 µm pore size and stored in a sterile amber bottle at 4 °C for further experiments.

2.2. Biosynthesis of Semiconductor and Metal/Semiconductor Nanoparticles

Zinc oxide nanoparticles (ZnO NPs) were prepared using cell-free filtrate (CFF) of *L. sphaericus*. Briefly, 250 ml of zinc nitrate (0.1 M) was used as metal ions precursor solution and taken in a 1000 ml Erlenmeyer flask, and 250 ml of bacterial filtrate was added dropwise while stirring at 40 °C for 1 h. This mixture was further stirred at 40 °C for 72 h. In another batch, to prepare silver/ZnO (Ag/ZnO) NPs, zinc nitrate (0.1 M) was mixed with silver nitrate (0.1 mM) and stirred at 40 °C for 72 h. Bacterial filtrate without zinc ions precursor solution was used as a negative control. After 72 h of incubation, the synthesized nanoparticles and nanocomposites were centrifuged at 10,000 rpm for 20 min, and the pellet was washed with deionized water and ethanol and dried overnight at 60 °C before calcined at 450 °C for 6 h. These biosynthesized nanoparticles and nanocomposites were further characterized for their physicochemical properties.

2.3. Characterization of ZnO and Ag/ZnO

The biosynthesized ZnO and Ag/ZnO were characterized by ultraviolet-visible spectroscopy using a UV-vis-NIR spectrophotometer (Varian CARY 5000, Agilent Technologies, CA, USA) between wavelengths 200 and 1100 nm. The functional groups of the CFF and their involvement in the synthesis of ZnO were analyzed by Fourier-transform infrared (FT-IR) spectroscopy (Model: Spectrum 100; Perkin Elmer) in the 400–4000 cm^{-1} range. The hydrodynamic size and the zeta potential were analyzed using a Zeta sizer (Model: Nano ZS90; Malvern Instruments, UK). The crystallinity of ZnO NPs was assessed by powder X-ray diffraction analysis (XRD) using PANalytical X'PertPRO MPD (Eindhoven, The Netherlands) scanned at 2θ values of 10° to 90° operated at 30 mA and 40 kV with a radiation source of Cu Kα ($\lambda = 1.54$ Å). The crystallite size of ZnO NPs was calculated by the Debye-Scherrer equation as follows: $D = 0.9\lambda/\beta\cos\theta$, where D is the crystallite size, 0.9 is the Scherrer's constant, λ is the X-ray wavelength, β is full width at half maximum (FWHM), and θ is Bragg diffraction angle (degrees). The morphology and the elemental composition of the ZnO and Ag/ZnO NPs were analyzed using a Field emission scanning electron microscope (FE-SEM) coupled to energy dispersive spectroscopy (EDX) (Model: S4800; Hitachi, Japan). To observe the high-resolution morphology and elemental composition of NPs, field emission-transmission electron microscopy (FE-TEM) with energy-dispersive X-ray spectroscopy (EDX) was performed using Tecnai G^2 F20 Twin TMP (Philips/FEI Company, USA) at an accelerating voltage of 200 kV. Photoluminescence (PL) spectroscopy was carried out using the Raman System (HORIBA Scientific, Japan) with a 325 nm He-Cd laser at 50 mW, and LabSpec 6 software was used for analysis.

2.4. Evaluation of the Antibacterial Activity of ZnO and Ag/ZnO NPs

The antibacterial activity of ZnO and Ag/ZnO NPs against gram-positive (*Staphylococcus aureus*) and gram-negative (*Escherichia coli*) bacteria was assessed using the agar well diffusion method and colony count method [20]. For the agar well diffusion method, overnight cultured bacterial cultures of *S. aureus* and *E. coli* cultured on TS broth were spread plated onto Muller Hinton (MH) agar medium, and agar wells were made using a sterile cork borer (8 mm). Different concentrations of biosynthesized ZnO and Ag/ZnO (200 and 400 µg; 40 µl) were added and incubated at 37 °C for 16 h. Ampicillin was used as a positive control, the zone of inhibitions (ZOIs) was measured, and the antibacterial activity was recorded. For the colony counting method, bacteria (3×10^8 CFU/ml) were

 doi:10.20944/preprints202307.0022.v1

exposed to ZnO and Ag/ZnO (200 and 400 µg/ml) and incubated at 37 °C for 3 h. The live bacterial colonies were counted by spread plating on TSA, and colony-forming units were calculated.

2.5. In Vitro Cytotoxicity Assay

2.5.1. Cell Culture

The HeLa cancer cell line was cultured in a 75 cm^2 flask using EMEM supplemented with 10% FBS (v/v) and 1% penicillin/streptomycin (w/v) at 95% humidified atmosphere air and 5% CO_2 at 37 °C. At 80% confluence, cells were harvested by trypsinization using 0.25% trypsin-EDTA and counted using trypan blue staining in a hemocytometer.

2.5.2. MTT Assay

The in vitro cytotoxicity of ZnO and Ag/ZnO against the HeLa cancer cell line was determined using the MTT assay. The HeLa cells (10,000 cells/well) were seeded onto 96 well plates and cultured for 3 days on an EMEM medium. After culturing, the old media was aspirated and replenished with new media containing different concentrations of ZnO and Ag/ZnO (1.56-100 µg/ml) and exposed for 24 and 48 h under specified conditions. After the treatment, MTT solution (0.5 mg/ml) was added to each well and incubated at dark for 4 h. The untreated wells were used as controls. Then, the supernatant was removed, the formazan was dissolved with DMSO, and the absorbance was read at 570 nm with a reference wavelength of 690 nm using an Epoch™ microplate spectrophotometer (BioTek Instruments, Vermont, USA). To determine the in vitro cytotoxicity, we calculated the percent cytotoxicity as % Cytotoxicity = 100 × (OD value of control – OD value of sample)/OD value of the control.

2.6. Photocatalytic Degradation of Methylene Blue Using ZnO and Ag/ZnO

The photocatalytic degradation of methylene blue (MB) by biosynthesized ZnO and Ag/ZnO as photocatalysts were assessed under simulated solar light irradiation [1]. Briefly, 100 ml of 0.001% (w/v) MB dissolved in deionized water was taken in a 250 mL conical beaker, and 0.1% (w/v) ZnO or Ag/ZnO was added and incubated in the dark at room temperature for 30 min to achieve adsorption-desorption equilibrium. Later, the mixture in a conical beaker was exposed to simulated solar irradiation using an Ultra-Vitalux lamp (300 W) at a 15 cm distance. For 120 min, samples were taken and centrifuged at 12,000 rpm for 10 min, and the absorbance of the supernatant was analyzed using a UV-vis spectrophotometer. The concentration of MB was quantified using the maximum absorbance (λ_{max}) of the solution at 665 nm. The degradation percentage of MB was calculated using the dye concentration after a particular time over the initial dye concentration as follows: Degradation (%) = $((C_0 - C_t)/C_0) \times 100$, where C_0 and C_t are the concentrations of dye at initial and specific time intervals, respectively.

3. Results and Discussion

3.1. Mechanism of Biological Synthesis of Semiconductor and Metal/Semiconductor Nanoparticles

The biological synthesis of metal oxide and metal/metal oxide nanoparticles as semiconductors and metal/semiconductor NPs can be achieved through plants, microorganisms, secondary metabolites, and biomacromolecules. The biological synthesis of these NPs in a greener method without toxic/hazardous chemicals at ambient conditions is sustainable and eco-friendly. The bottom-up approach of arranging atoms into nuclei, followed by the formation of nanoparticles, is widely used. Among different greener routes, microbe-mediated extracellular synthesis involving the oxidation/reduction of metallic ions by bacterial or fungal enzymes and their biomolecules is more advantageous. Oxidoreductase enzymes such as NADH-dependent nitrate reductases are mainly involved in the biocatalytic synthesis of metal or metal oxide NPs [12]. The reaction between the bioreducing enzymes/biomolecules and Zn^{2+} ions from the metal ion precursor forms ZnO NPs.

Preprints (www.preprints.org) | NOT PEER-REVIEWED | Posted: 3 July 2023 doi:10.20944/preprints202307.0022.v1

Various biomolecules, such as sugars and proteins, can also act as stabilization molecules. In the formation of Ag/ZnO NPs, the silver nanoparticles (Ag NPs) are formed by the reduction of Ag^+ ions by the proteins/sugars of cell-free filtrate (CFF) on the surface of ZnO NPs forming Ag/ZnO NPs [21].

The formation of biosynthesized ZnO and Ag/ZnO NPs was initially confirmed by the visual assessment. The color of the reaction mixture was changed from clear pale-yellow color to turbid pale yellow-whitish color for ZnO and brownish color for Ag/ZnO. These characteristic colors indicate the formation of ZnO precipitate and Ag NPs on ZnO. The enzymes, biomacromolecules, and bioactive metabolites on the CFF of *L. sphaericus* are presumed to be involved in forming and stabilizing ZnO and Ag/ZnO NPs (Figure 1). Jain et al. [22] demonstrated the synthesis of white precipitate ZnO NPs using zinc-tolerant bacteria *Serratia nematodiphila* by reduction process [22]. The rhamnolipids (RLs) of *Pseudomonas aeruginosa* and the phycocyanin pigment of cyanobacteria are also involved in synthesizing ZnO NPs [23,24]. The metabolites of *Bidens pilosa* and *Verbascum speciosum* plant extracts are also involved in the green synthesis of Ag/ZnO nanocomposites with antimicrobial and anticancer activities [25,26].

Figure 1. Schematic diagram of the biosynthesis of ZnO (semiconductor) and Ag/ZnO (metal/semiconductor) nanoparticles using the cell-free filtrate (CFF) of *L. sphaericus*.

3.2. Characterization of Biosynthesized ZnO and Ag/ZnO NPs

Figure 2a shows the UV-vis spectra of ZnO and Ag/ZnO NPs. When treating the metal precursors with CFF, zinc ions form ZnO NPs, and Ag^+ ions form Ag NPs by reacting with bacterial enzymes and the bioactive molecules. The formation of ZnO and Ag/ZnO NPs was investigated by UV-vis diffuse reflectance spectroscopy (UV-Vis DRS). ZnO shows a maximum absorption band in the UV region at ~366 nm, which agrees with the previous reports [1]. The formation of Ag NPs on ZnO NPs in the production of Ag/ZnO was confirmed by the broad absorbance in the visible region for Ag NPs in the range of 450 to 550 nm. The formation of Ag NPs on ZnO causes a broad absorption band in the visible region due to the surface plasmon resonance (SPR) of polydispersed anisotropic Ag NPs [27]. The excitation of the Ag/ZnO NPs causes the generation of more electron-hole pairs resulting in the broadening of the absorption peak [28]. The intensity and position of the SPR band of Ag NPs are correlated with the size, shape, composition, and local environment. Similar results were reported in the biogenic synthesis of Ag/ZnO NPs using the extracts of *Bidens pilosa* and *Crataegus monogyna* [25,29].

Preprints (www.preprints.org) | NOT PEER-REVIEWED | Posted: 3 July 2023 doi:10.20944/preprints202307.0022.v1

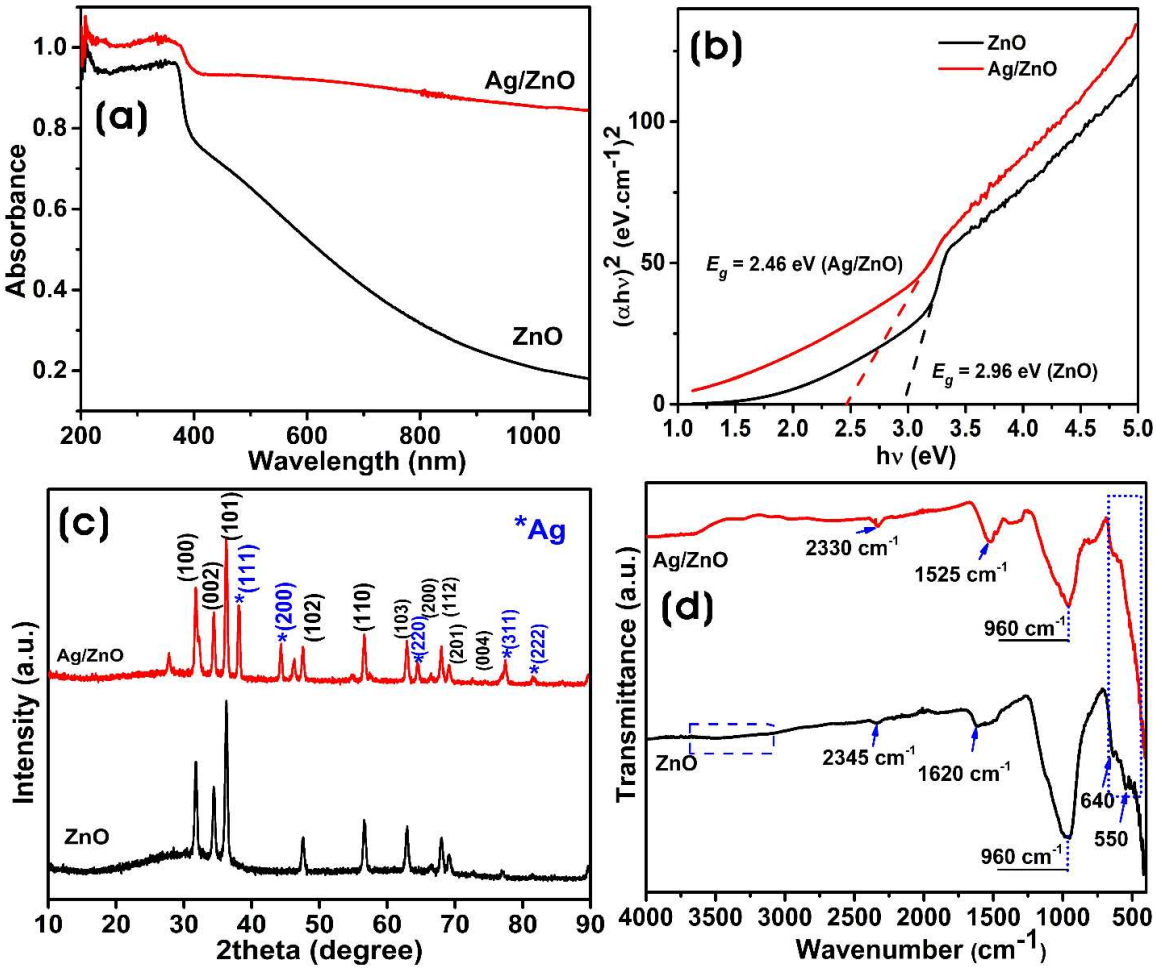

Figure 2. (**a**) UV–Vis DRS spectra, (**b**) Tauc plot, (**c**) XRD pattern, and (**d**) FTIR spectra of biosynthesized ZnO and Ag/ZnO NPs.

The band gap energy (Eg) is the energy required to excite electrons from the valence band to the conduction band. The direct band gap energies of biosynthesized ZnO and Ag/ZnO NPs are calculated using the Tauc equation: $\alpha h\nu = A(h\nu - Eg)^n$; where α is the optical absorption coefficient, h is Planck constant; ν is the photon's energy; A is the constant; and Eg is the band gap energy. The Eg is determined using the optical absorption coefficient from the experimental absorbance. The extrapolation of the linear region of the curve to the X-axis gives the Eg values [30]. Figure 2b shows the Eg values of ZnO and Ag/ZnO NPs. The optical band gap energies of biosynthesized ZnO and Ag/ZnO NPs were 2.96 eV and 2.46 eV, respectively. ZnO can absorb light less than 400 nm, which is mainly in the UV region, hindering its visible light photocatalytic applications. With the binding of Ag NPs on the surface of ZnO NPs, there was a decrease in the band gap energy of Ag/ZnO and utilized visible light absorption of more photons. The heterogeneous structure of Ag NPs on ZnO allows the visible-light-induced activation due to the localized SPR of Ag NPs and enables the absorption of the whole solar spectrum. Thus, the band gap modification of ZnO through silver doping extends the absorption of light in the visible wavelength. The high intensity and broad absorption peak of Ag/ZnO NPs through the entire solar spectrum can also facilitate the enhanced light absorption capacity both in UV and visible regions for photocatalytic activities [31]. The band gap energy of Ag/ZnO is lower than that of ZnO. The decrease of optical band gap energy can be influenced by factors such as grain size, carrier concentration, structural parameters, lattice strain, and the existence of defects or impurities [32,33].

The crystallite size, crystallinity, and purity of nanoparticles and nanocomposites were investigated by XRD analysis. Figure 2c shows the XRD pattern of biosynthesized ZnO and Ag/ZnO

 doi:10.20944/preprints202307.0022.v1

NPs. The XRD peaks of biosynthesized ZnO NPs appeared at 31.7°, 34.39°, 36.28°, 47.60°, 56.57°, 62.81°, 66.44°, 68.08°, 69.37, and 72.7° corresponding to (100), (002), (101), (102), (110), (103), (200), (112), (201), and (004) lattice of the hexagonal phase of wurtzite ZnO (JCPDS No. 036-1451) without any impurities after calcination. The presence of Ag NPs in Ag/ZnO NPs was confirmed by the diffraction peaks at 38.10°, 44.29°, 64.42°, 77.38°, and 81.52° corresponding (111), (200), (220), (311), and (222) to the face-centered cubic (fcc) silver phase (JCPDS number 2-109), which confirms the presence of silver along with the diffraction peaks of ZnO on the Ag/ZnO NPs [1]. The silver ions (0.122 nm) are larger than the zinc ions (Zn^{2+}); silver ions cannot substitute in the ZnO matrix; thus, they can only be formed over the surface of ZnO [34]. The crystallite size of ZnO and Ag NPs in Ag/ZnO NPs calculated using the Debye-Scherrer equation was 25.6 ± 9.9 nm and 24.9 ± 1.9 nm, respectively. Similarly, the crystallinity of ZnO and Ag/ZnO was 93.53 % and 93.48%, respectively. The decrease in the intensity of diffraction peaks of ZnO in Ag/ZnO indicated a slight reduction in the crystalline structure of Ag/ZnO.

The presence of functional groups from the cell-free filtrate (CFF) of *L. sphaericus* used in the biosynthesis and stabilization of ZnO and Ag/ZnO was investigated using FTIR analysis in the range of 400–4000 cm^{-1} (Figure 2d). The infrared absorption spectra of ZnO and Ag/ZnO NPs showed similar spectra, and the stretching vibration of the O–H bond of the H_2O molecule in the Zn–O lattice around 3400 cm^{-1} almost disappeared after calcination [35]. The absorption band around 2330 and 2345 cm^{-1} could have resulted from the CO_2 adsorption on the surface of ZnO and Ag/ZnO, respectively. The peak around 1620 cm^{-1} in ZnO was ascribed to H–O–H bending vibrations due to the water molecule [36]. The intense band at 960 cm^{-1} was correlated to the deformation of bands of C=O [37]. The broad IR band around 400–600 cm^{-1} was attributed to the distinct stretching vibration mode for the metal-oxygen bond, confirming the ZnO bond formation [38].

Dynamic light scattering (DLS), also known as photon correlation spectroscopy, measures the Brownian motion of particles in solution and relates it to the size of particles. DLS is a rapid technique to find the average size and distribution of NPs. Generally, DLS measures the hydrodynamic radius, which is influenced by the structure, shape, and surface properties of the NPs. Ag/ZnO shows an increase in the size of the NPs than ZnO, which could be due to Ag NPs forming on the surface of ZnO and by aggregation. Zeta (ζ) potential measurements are used to evaluate the surface charges of NPs. The NP's stability is directly correlated to the magnitude of the zeta potential charge. ZnO and Ag/ZnO particles dispersed in an aqueous solution were used for the zeta potential measurements. The zeta potential values of colloidal particles are directly correlated with their stabilities. The higher zeta potential value indicates better physical colloidal stability. The colloidal particles with ζ values between ±10 and ±30 are considered incipiently stable, and those with ±30 and ±40 are considered moderately stable. The zeta potential values of ZnO and Ag/ZnO NPs were –30.1 ± 8.39 and –29 ± 5.74 mV, respectively, indicating the negatively charged biomacromolecules of CFF of *L. sphaericus* are involved in stabilization (Supplementary Figure S1).

FE-SEM was used to observe the surface morphology of ZnO and Ag/ZnO NPs. ZnO NPs synthesized by the precipitation method using the CFF of *L. sphaericus* as an additive promoted the formation of puffy-like morphology (Figure 3a–d). The addition of sustainable and eco-friendly materials as additives directs the formation of ZnO with unique morphology [39]**.** The calcination process at different temperatures also influences the formation of different morphologies [40]**.** The puffy-like morphology of ZnO NPs was anisotropic and polydispersed on a submicronic scale. The agglomeration of ZnO was presumed to have been caused by the higher surface area and affinity among NPs. In the case of Ag/ZnO, the addition of silver nitrate into the CFF-treated zinc nitrate mixture resulted in the formation of irregularly shaped polydispersed ZnO particles with nano-dimensioned Ag NPs on its surface.

Preprints (www.preprints.org) | NOT PEER-REVIEWED | Posted: 3 July 2023 doi:10.20944/preprints202307.0022.v1

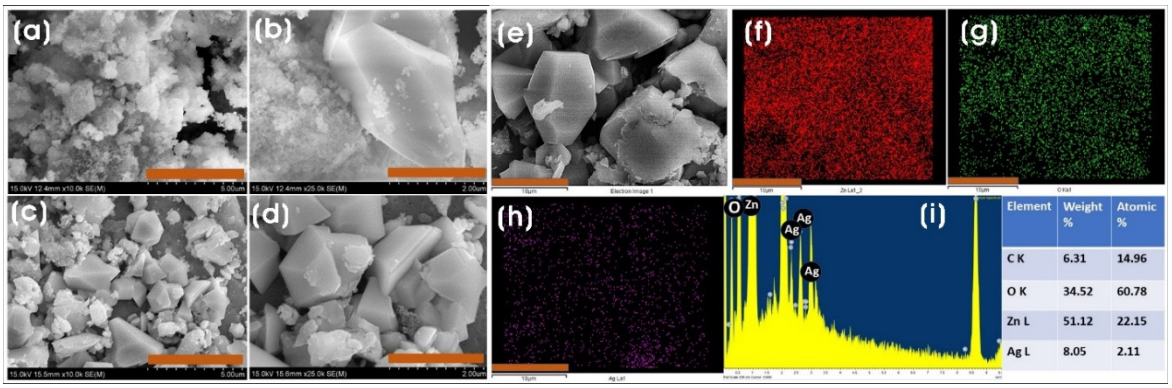

Figure 3. FE-SEM images of (**a**–**c**) ZnO and (**d**–**f**) Ag/ZnO NPs at different magnifications. Scale bars, (**a**) 10 µm, (**b**,**d**,**e**) 5 µm, and (**c**,**f**) 2 µm. (**e**) FE-SEM-EDX micrograph of Ag/ZnO NP and elemental maps of (**f**) Zn-L, (**g**) O-K, (h) Ag-L, and (**i**) EDX spectrum and the table with elemental composition. Scale bars, (**e**–**h**) 10 µm.

The FE-SEM-EDX analysis was performed to investigate the elemental composition of ZnO and Ag/ZnO NPs. The EDX spectra and the elemental mapping with the quantified elemental composition of ZnO and Ag/ZnO NPs are shown in Supplementary Figure S2 and Figure 3e–i, respectively. The EDX spectrum of ZnO showed oxygen (O-Kα) peak at low energy (0.560 keV) and Zn-Lα, Zn-Kα, and Zn-Kβ peaks of zinc element at ~1.01, 8.6, and 9.5 keV, respectively. Whereas Ag/ZnO spectra showed the presence of silver element peaks viz Ag-Kα, Ag-Lα, Ag-Lβ, and Ag-Lβ2 peaks at ~2.6, 3.1, 3.26, and 3.35 keV, respectively, along with the Zn, and O peaks, which infers that silver was successfully incorporated as Ag NPs in forming Ag/ZnO NPs.

Figure 4a–d shows the FE-TEM images of biosynthesized Ag/ZnO NPs at different magnifications. FE-TEM images verified the formation of puffy-like ZnO NPs and the attachment of Ag NPs on the surface of ZnO. It was found that nanosized spherical and quasi-spherical Ag NPs (dark spots) were attached to the submicronic irregularly shaped puffy-like ZnO particles. High-angle annular dark field (HAADF) STEM image of the biosynthesized Ag/ZnO NC shows that Ag NPs are formed on the surface of ZnO. The elemental composition analysis by EDX line scan confirmed the presence of silver element on the presumed Ag NPs particles on ZnO (Figure 4e–h).

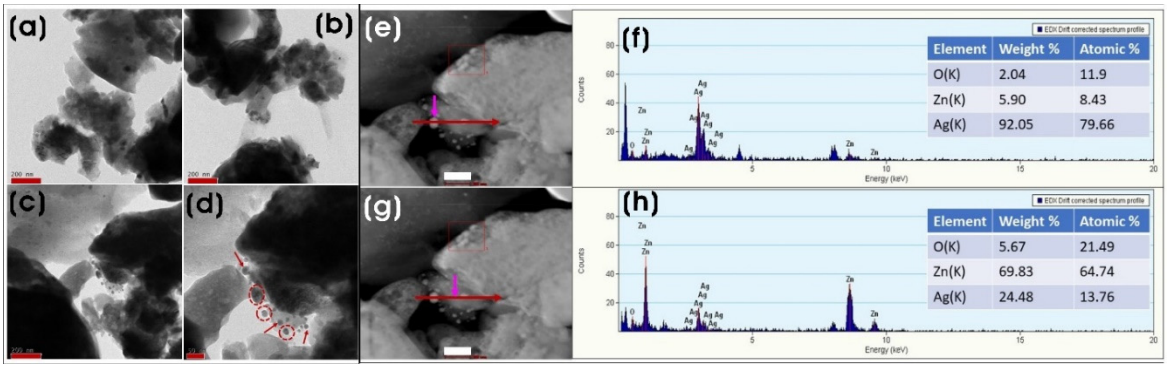

Figure 4. FE-TEM images of biosynthesized Ag/ZnO NPs at different magnifications. Scale bars, (**a**–**c**) 200 nm and (**d**) 50 nm. (**e**,**g**) HAADF-STEM images and EDX line scan maps of the arrow-indicated areas (inset shows the table of elemental composition). Scale bar, (**e**,**g**) 100 nm.

Photoluminescence (PL) is an essential technique for analyzing biosynthesized ZnO and Ag/ZnO NPs due to their visible PL nature. ZnO interacts with light and undergoes photogeneration of electron-hole (e^-/h^+) pairs that subsequently recombine radiatively, giving rise to PL spectra. The emission spectrum of ZnO comprises near-band edge (NBE) emission and deep-level emission (DLE). The defects or the presence of foreign impurities in the ZnO can change the PL outcome. Figure 5a

Preprints (www.preprints.org) | NOT PEER-REVIEWED | Posted: 3 July 2023 doi:10.20944/preprints202307.0022.v1

shows the PL spectra of ZnO and Ag/ZnO NPs at room temperature. A typical peak in the visible region of ~480 nm comes from oxygen vacancies and other defects of ZnO nanostructures [41]. Both show the predominant emission only in the DLE mode around 400–700 nm and almost no emission in the NBE region below 400 nm. The low NBE peak confirms that ZnO was granularly textured and exhibits low optical quality. The presence of DLE indicates the presence of deep-level radiative defects [42]. The addition of silver to ZnO NPs results in the formation of Ag/ZnO NPs with increased e^-/h^+ lifetime and subsequent reduction in their recombination rate [43,44]. Also, the intensity of the broad visible defect emission decreases with the addition of Ag with ZnO, which also indicates the separation of photoinduced e^-/h^+ pairs and prolonged recombination of photoinduced pairs due to the metal-semiconductor diode effect between Ag NPs and ZnO NPs in Ag/ZnO [45]. Ag/ZnO NCs produced by goji berry extract show decreased PL intensity in the UV emission compared to ZnO, indicating a decrease in the e^-/h^+ recombination rate and efficient charge separation [1].

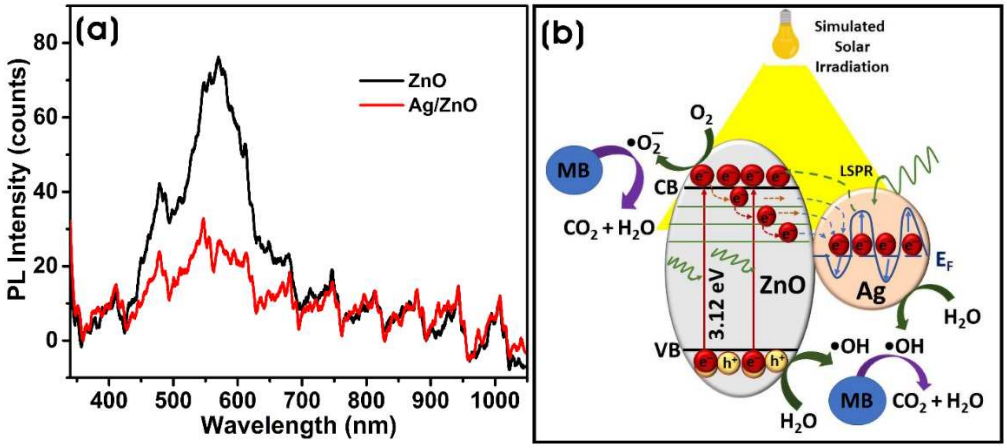

Figure 5. (**a**) Photoluminescence (PL) spectra of biosynthesized ZnO and Ag/ZnO NPs. (**b**) Schematic illustration of the photodegradation of methylene blue (MB) by biosynthesized Ag/ZnO NPs.

3.3. Applications of Biosynthesized ZnO and Ag/ZnO NPs

3.3.1. Photocatalytic Degradation

The photocatalytic efficiency of biosynthesized ZnO and Ag/ZnO NPs in methylene blue (MB) degradation, the cationic azo dye, has been investigated under simulated solar light. Figure 6a and 6b shows the UV-Vis absorption spectra of the photodegradation of MB with biosynthesized ZnO and Ag/ZnO NPs with time. The decolorization of the dye solution is the visible confirmation of the degradation of the dye. UV-Vis spectra of the reaction mixture containing dye and biosynthesized ZnO or Ag/ZnO NPs irradiated with simulated solar light were recorded at different intervals. The degradation of MB dye was monitored with the decrease in the intensity of the λ_{max} (665 nm) of the MB. The efficiency of photocatalysis is dependent on the properties of the photocatalyst material. The photocatalysis occurs on the surface of the photocatalyst, therefore by increasing the surface-to-volume ratio, manipulating the band structure of the photocatalyst, and limiting the recombination of photogenerated pairs can improve the photocatalytic performance of the photocatalyst nanomaterial [43,46,47]. Figure 6c shows the photocatalytic degradation graph of MB with time by ZnO and Ag/ZnO, i.e., C_t/C_0 versus time, where C_0 and C_t are the concentrations of MB at the initial time and time intervals "t," respectively. The reaction mixture containing photocatalyst (0.1% w/v) and MB (1 mg/100 ml) was incubated in the dark for adsorption-desorption equilibrium for 30 min, which shows that MB concentrations of 20.29 ± 0.91% and 2.32 ± 1.32%, were adsorbed on the photocatalyst ZnO and Ag/ZnO, respectively. The incorporation of silver into the ZnO decreased the adsorption of MB to the surface of Ag/ZnO than ZnO. However, despite the decrease in the adsorption of MB by Ag/ZnO in the dark, there was a significant increase in its photocatalytic degradation capacity [48]. Ag/ZnO showed 90.7 ± 0.91% photocatalytic degradation, which is more robust than ZnO with a 50.7 ± 0.53% photodegradation potential for 120 min (Figure 6d). The

Preprints (www.preprints.org) | NOT PEER-REVIEWED | Posted: 3 July 2023 doi:10.20944/preprints202307.0022.v1

photocatalytic degradation of MB by Ag/ZnO was significantly higher than ZnO NPs, and the enhanced degradation was due to the presence of Ag as a dopant in the ZnO lattice. The addition of silver enhances the photodegradation potential of Ag/ZnO NPs. The addition of Ag NPs as a dopant on the ZnO acts as an electron trapper. It decreases the recombination capacity of photogenerated electron-hole pairs and thereby increases carrier lifespan, enhancing photocatalytic efficiency [49].

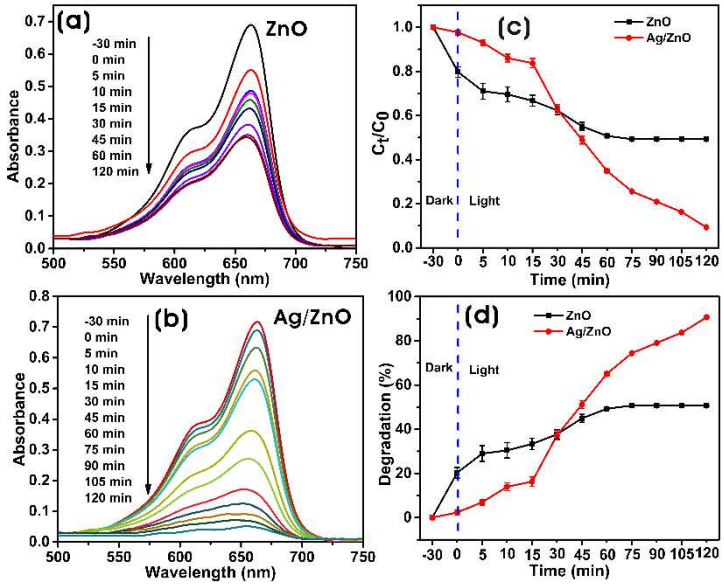

Figure 6. UV-vis absorbance spectra of the photodegradation of MB by biosynthesized (**a**) ZnO and (**b**) Ag/ZnO NPs. (**c**) The plot of C_t/C_0 versus time and (**d**) the degradation percentage of MB by biosynthesized ZnO and Ag/ZnO NPs.

3.3.1.1. Mechanism of Photocatalytic Degradation

Generally, reactive oxygen species (ROS) degrade several organic pollutants through redox reactions. The generation of electron–hole pair (e^-/h^+) reacts with molecular oxygen (O_2) and water molecules resulting in the production of ROS such as superoxide anion radicals ($^\bullet O_2^-$) and hydroxyl radicals ($^\bullet$OH), which are involved in the degradation and mineralization of pollutants to CO_2 and water [50]. Ha et al. [49] demonstrated that the photogenerated electrons (e^-) by Ag/ZnO propound the photocatalytic efficiency of the nanomaterial was due to the Schottky barrier formation of the composite and the localized SPR effect of the anisotropic Ag NPs. The photogenerated holes (h^+) also react with water molecules to yield hydroxyl radicals, which also involves the photocatalytic degradation of MB. Figure 5b depicts the proposed photocatalytic mechanism in the degradation of MB by biosynthesized Ag/ZnO NP under simulated solar irradiation.

The activation of Ag/ZnO NP by the incident photon energy causes the excitation of electrons of ZnO from the valence band (VB) to the conduction band (CB). Later these electrons are trapped in the defect states of ZnO and migrate to the Ag NPs as the CB energy level is higher than silver's Fermi level (EF). The visible light of the incident light also causes the localized SPR effect on Ag NPs, which excites Ag electrons to a higher excitation level and causes migration to the CB of ZnO due to the energy level difference. This significantly hinders the recombination of e^-/h^+ pairs and causes the accumulation of electrons on the CB of ZnO and holes on the VB of ZnO and Ag NPs. These accumulated electrons on the CB of ZnO reduce the O_2 adsorbed on the surface of the photocatalyst to generate $^\bullet O_2^-$, which further undergoes intermediate reactions with water molecules to produce $^\bullet$OH radicals. On the other hand, the holes also produce $^\bullet$OH radicals by oxidizing OH^-. All these generated ROS involved in decomposing a cationic azo dye, MB.

Preprints (www.preprints.org) | NOT PEER-REVIEWED | Posted: 3 July 2023 doi:10.20944/preprints202307.0022.v1

3.3.2. In Vitro Cytotoxicity Assay

Exposure to all concentrations of biosynthesized ZnO and Ag/ZnO (100-1.56 µg/ml) significantly induced cytotoxicity in a concentration-dependent and time-dependent manner on HeLa cancer cells. The highest cytotoxicity for ZnO NPs was 42.26 ± 2.23% on HeLa, whereas Ag/ZnO NPs exhibited 50.5 ± 0.15% at a concentration of 100 µg/ml after 48 h of exposure (Figure 7(I)). Compared to Ag/ZnO, ZnO NPs were found to be less cytotoxic against HeLa cancer cells. The elevated cytotoxicity of nanoparticles against HeLa cells with time and concentration occurs due to the highest uptake of nanoparticles by the cancer cells and their increased ROS generation inhibiting the transcriptional process [51]. Silver nanoparticles of Ag/ZnO NPs were reported to cause cytotoxicity to cancer cells through lipid peroxidation, protein thiol oxidation, and necrosis. In contrast, silver ions can cause H_2O_2 elevation and drive oxidative stress and apoptotic cell death [52]. Biogenic ZnO NPs synthesized using *Pandanus odorifer* leaf extract exhibited cytotoxicity against various cancer cells (MCF-7, HepG2, and A-549) at a concentration from 50–100 µg/ml [53]. Chandrasekaran et al. [54] prepared ZnO NPs using the *Vinca rosea* leaves extract, which showed potent cytotoxic activity against MCF-7 cells. Similarly, Tanino et al. [55] reported that the anticancer activity of ZnO NPs was exhibited by inducing highly reactive ROS, DNA leakage from nuclei by membrane rupture, apoptosis, and necrosis. The morphological properties of ZnO NPs are also extensively involved in the anticancer activity of ZnO NPs. It was found that spherical ZnO NPs at 100 µg/ml showed better anticancer activity than hexagonal and rod-like NPs [56]. In our study, Ag/ZnO NPs act as a strong anticancer agent compared to ZnO NPs. Rafique et al. [18] also demonstrated that ZnO/Ag NPs produced by *Moringa oleifera* exhibited strong anticancer activity in HeLa cells. Moreover, cyclodextrin-Ag NPs decorated titanium dioxide (TiO_2-Ag NPs @CD) also induced superior cytotoxicity at a concentration of 64 µg/ml on HeLa cells. The disintegration of cell membranes and the production of ROS causing oxidative stress are involved in the anticancer properties of these NCs [57].

Figure 7(II) shows the live (green) and dead (red) cells of HeLa cancer cells after exposure to biosynthesized ZnO and Ag/ZnO for 48 h. The combined use of calcein and propidium iodide in dual fluorescence assay allows the evaluation of cellular viability and cell death of HeLa cancer cells. The microscopic fluorescent images of HeLa cells exposed to nanoparticles for 48 h concur with the results of the MTT assay. The nonfluorescent calcein AM dye was converted into green, fluorescent calcein dye by the intracellular esterase activity of the live cell, whereas the propidium iodide red fluorescence increases by intercalating to the nucleic acid of the dead cells [58].

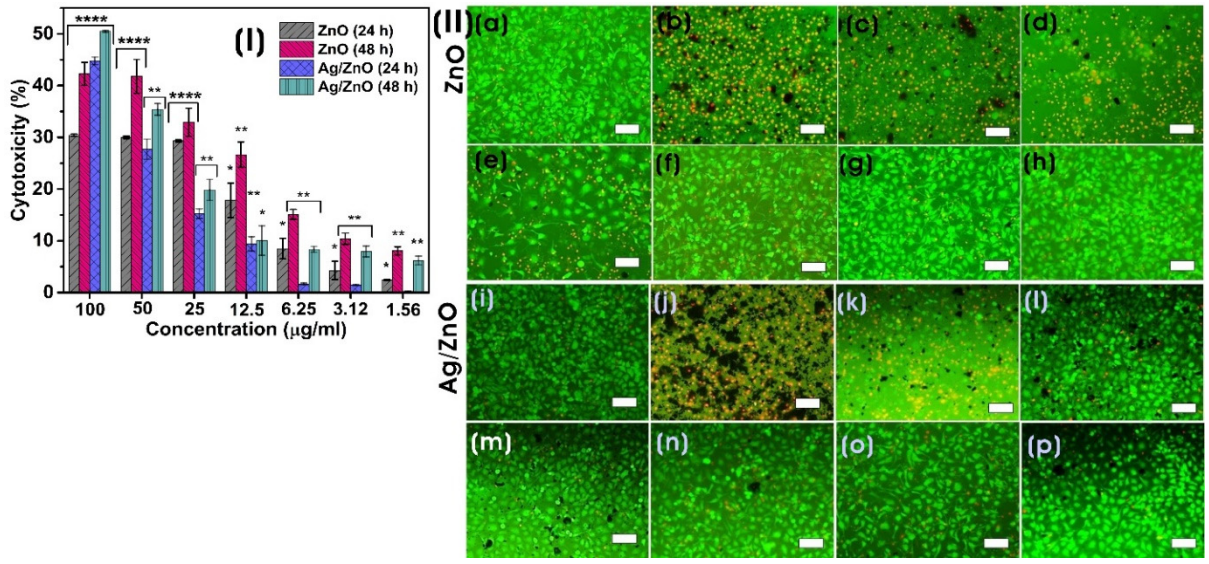

Figure 7. (**I**) In vitro cytotoxicity of biosynthesized ZnO and Ag/ZnO NPs on human cervical cancer HeLa cells for 24 and 48 h. Data are expressed as mean ± SD (three replicates). The significances of difference between cytotoxicity of different concentrations of NPs with control at 24 and 48 h were

Preprints (www.preprints.org) | NOT PEER-REVIEWED | Posted: 3 July 2023 doi:10.20944/preprints202307.0022.v1

determined by two-tailed unpaired Welch's t-test (*$P \leq 0.05$; **$P \leq 0.01$; ***$P \leq 0.001$; ****$P \leq 0.0001$). (**II**) Live/dead staining assay of HeLa cancer cells on exposure to biosynthesized ZnO and Ag/ZnO NPs after 48 h (scale bar: 100 µm). (**a**,**i**) control, (**b**,**j**) 100 µg/ml, (**c**,**k**) 50 µg/ml, (**d**,**l**) 25 µg/ml, (**e**,**m**) 12.5 µg/ml, (**f**,**n**) 6.25 µg/ml, (**g**,**o**) 3.12 µg/ml, and (**h**,**p**) 1.56 µg/ml of ZnO and Ag/ZnO NPs, respectively.

3.3.3. Antibacterial Assay

The antibacterial activity of biosynthesized ZnO and Ag/ZnO NPs is shown in Figures 8a and 8b. The agar well-diffusion method shows that both Gram-negative (*E. coli*) and Gram-positive (*S. aureus*) were inhibited largely by Ag/ZnO NPs, and ZnO did not show any profound antibacterial activity. Moreover, *E. coli* showed slight resistance to Ag/ZnO compared to *S. aureus*. The antibacterial activity of NPs could also be influenced by the shape, size, surface charge, and surface functionalization [59,60]. The ZOIs for Ag/ZnO were 9.95 ± 0.588 (200 µg), 10.35 ± 0.31 (400 µg) and 12.12 ± 0.65 (200 µg), 12.48 ± 0.509 (400 µg) towards *E. coli* and *S. aureus*, respectively, whereas the ZOI of control was 12.18 ± 1.47 (500 µg) and 31.42 ± 1.05 mm (300 µg) for *E. coli* and *S. aureus*, respectively. The colony-forming units (CFU) assay method was used to evaluate the effect of biosynthesized ZnO and Ag/ZnO NPs on *E. coli* and *S. aureus* in solution. After 3 h of exposure to different concentrations of NPs (250–62.5 µg/ml), it was found that Ag/ZnO showed higher antibacterial activity compared to ZnO (Figures 8c and 8d). All concentrations of NPs showed significant antibacterial activity towards both *E. coli* and *S. aureus*. Compared to *E. coli*, *S. aureus* showed highly significant susceptibility to the antibacterial activity of Ag/ZnO NPs at all concentrations. Nevertheless, at a concentration of 250 µg/ml, Ag/ZnO NPs showed complete bactericidal activity in both *E. coli* and *S. aureus* than ZnO NPs. The antibacterial activity of Ag/ZnO was due to the synergistic effect of Ag and ZnO as well as the production of high levels of ROS generation [61,62]. The oxidative stress caused by ROS generation also plays a crucial role in the inhibition of bacterial growth. The interaction of metal nanoparticles with the bacterial membrane results in the loss of membrane integrity and oxidation of membrane lipids causing adverse effects on the bacteria. Moreover, Ag NPs or Ag/ZnO also triggers the production of hydroxyl radical and singlet oxygen, causing aberration in the cell membrane components and leading to bacterial death [7].

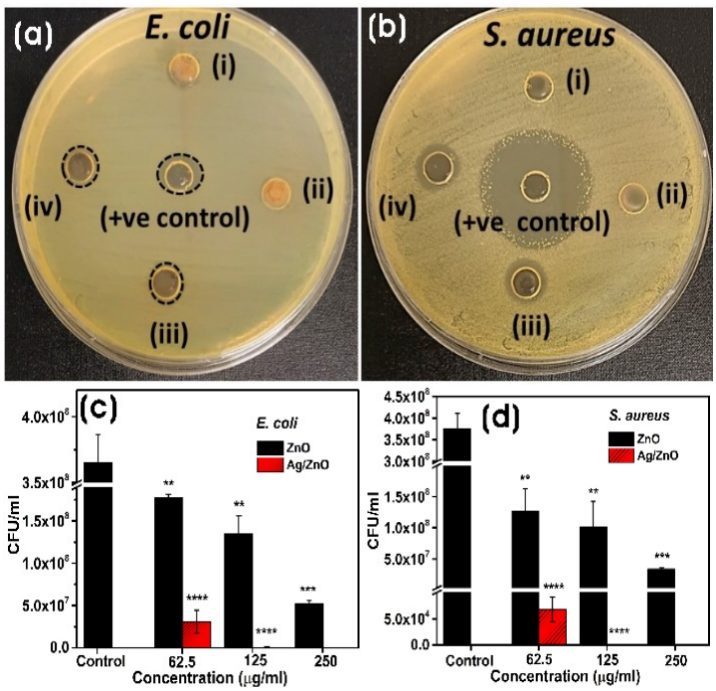

Figure 8. Antibacterial activity of biosynthesized ZnO and Ag/ZnO NPs against *E. coli* and *S. aureus*. (**a**,**b**) agar-well diffusion assay with (i) ZnO (200 µg), (ii) ZnO (400 µg), (iii) Ag/ZnO (200 µg) and (iv) Ag/ZnO (400 µg), and (**c**,**d**) bacterial colony counting assay at different concentrations. The results are

means ± SD of three replicates. The significance of the difference between control and bacteria treated with different concentrations of nanoparticles was determined by two-tailed unpaired Welch's t-test (**$P \leq 0.01$; ***$P \leq 0.001$; ****$P \leq 0.0001$).

4. Conclusions

In this paper, we successfully biosynthesized ZnO and Ag/ZnO NPs by the environmentally benign greener route using the cell-free filtrate of *L. sphaericus*. The formation of biosynthesized ZnO NPs was irregularly shaped puffy-like submicronic particles. The spherical and quasi-spherical Ag NPs were embedded on the surface of ZnO NPs. These semiconductor and metal/semiconductor nanoparticles showed excellent antibacterial, anticancer, and photocatalytic degradation capabilities. The photocatalytic degradation efficiency of Ag/ZnO was higher than ZnO, exhibiting the improved separation and lifetime of photogenerated electron/hole pairs. The addition of Ag to ZnO contributed to the increased decomposition of methylene blue up to 90.7 % in 120 minutes. These biosynthesized NPs also exhibited significant antibacterial activity against *E. coli* and *S. aureus* and anticancer activity against HeLa cervical cancer cells. Hence, these biologically synthesizing strategies of semiconductor nanomaterials can be used for biomedical and environmental applications.

Supplementary Materials: The following supporting information can be downloaded at the website of this paper posted on Preprints.org.

Acknowledgments: This research was supported by the Korea Basic Science Institute (National Research Facilities and Equipment Center) grant funded by the Ministry of Education. This research was supported by the National Research Foundation of Korea (NRF) (Grant No.2020R1A6A1A03044512 & No.2019R1A6C1010046). Authors also thank the Korea Institute of Planning and Evaluation for Technology in Food, Agriculture, and Forestry (IPET) through the High Value-added Food Technology Development Program, funded by the Ministry of Agriculture, Food and Rural Affairs (MAFRA) (321027–5). The characterization instruments were utilized at the Core Research Support Center for Natural Products and Medical Materials (CRCNM) at Yeungnam University.

CRediT Authors Contributions**:** Conceptualization: KBN; Funding Acquisition: SSH; Writing- Original Draft Preparation: KBN, RB, YJS, SSH; Writing—Review and Editing: KBN, RB, YJS, SSH

Declaration of Competing Interest: The authors declare that they have no known competing financial interests or personal relationships that could have appeared to influence the work reported in this paper.

References

1. Sharwani, A.A.; Narayanan, K.B.; Khan, M.E.; Han, S.S. Photocatalytic degradation activity of goji berry extract synthesized silver-loaded mesoporous zinc oxide (Ag@ ZnO) nanocomposites under simulated solar light irradiation. *Scientific Reports* **2022**, *12*, 10017.
2. Castro, A.M.; Nogueira, V.; Lopes, I.; Rocha-Santos, T.; Pereira, R. Evaluation of the potential toxicity of effluents from the textile industry before and after treatment. *Applied Sciences* **2019**, *9*, 3804.
3. Cova, T.F.; Pais, A.A.; Seixas de Melo, J.S. Reconstructing the historical synthesis of mauveine from Perkin and Caro: procedure and details. *Scientific reports* **2017**, *7*, 6806.
4. Perkin, W. Producing a new coloring matter for dyeing with a lilac or purple color stuffs of silk, cotton, wool, or other materials. *William Henry Perkin, United Kingdom, BP1984* **1856**.
5. Mondal, S.; Samanta, G.; De la Sen, M. Dynamics of Oxygen-Plankton Model with Variable Zooplankton Search Rate in Deterministic and Fluctuating Environments. *Mathematics* **2022**, *10*, 1641.
6. Kasperchik, V.; Yaskevich, A.; Bil'Dyukevich, A. Wastewater treatment for removal of dyes by coagulation and membrane processes. *Petroleum Chemistry* **2012**, *52*, 545-556.
7. Zhang, J.; Wang, F.; Yalamarty, S.S.K.; Filipczak, N.; Jin, Y.; Li, X. Nano silver-induced toxicity and associated mechanisms. *International Journal of Nanomedicine* **2022**, 1851-1864.
8. Chandran, H.; Meena, M.; Sharma, K. Microbial biodiversity and bioremediation assessment through omics approaches. *Frontiers in Environmental Chemistry* **2020**, *1*, 570326.
9. Patel, H.; Yadav, V.K.; Yadav, K.K.; Choudhary, N.; Kalasariya, H.; Alam, M.M.; Gacem, A.; Amanullah, M.; Ibrahium, H.A.; Park, J.-W. A recent and systemic approach towards microbial biodegradation of dyes from textile industries. *Water* **2022**, *14*, 3163.

10. Talha, M.A.; Goswami, M.; Giri, B.; Sharma, A.; Rai, B.; Singh, R. Bioremediation of Congo red dye in immobilized batch and continuous packed bed bioreactor by Brevibacillus parabrevis using coconut shell bio-char. *Bioresource technology* **2018**, *252*, 37-43.
11. Narayanan, K.B.; Sakthivel, N. Biological synthesis of metal nanoparticles by microbes. *Advances in colloid and interface science* **2010**, *156*, 1-13.
12. Narayanan, K.B.; Sakthivel, N. Green synthesis of biogenic metal nanoparticles by terrestrial and aquatic phototrophic and heterotrophic eukaryotes and biocompatible agents. *Advances in colloid and interface science* **2011**, *169*, 59-79.
13. Mao, T.; Liu, M.; Lin, L.; Cheng, Y.; Fang, C. A Study on Doping and Compound of Zinc Oxide Photocatalysts. *Polymers* **2022**, *14*, 4484.
14. Harish, S.; Archana, J.; Sabarinathan, M.; Navaneethan, M.; Nisha, K.; Ponnusamy, S.; Muthamizhchelvan, C.; Ikeda, H.; Aswal, D.; Hayakawa, Y. Controlled structural and compositional characteristic of visible light active ZnO/CuO photocatalyst for the degradation of organic pollutant. *Applied Surface Science* **2017**, *418*, 103-112.
15. Yu, C.; Yang, K.; Xie, Y.; Fan, Q.; Jimmy, C.Y.; Shu, Q.; Wang, C. Novel hollow Pt-ZnO nanocomposite microspheres with hierarchical structure and enhanced photocatalytic activity and stability. *Nanoscale* **2013**, *5*, 2142-2151.
16. Kareem, M.; Bello, I.; Shittu, H.; Sivaprakash, P.; Adedokun, O.; Arumugam, S. Synthesis, characterization, and photocatalytic application of silver doped zinc oxide nanoparticles. *Cleaner Materials* **2022**, *3*, 100041.
17. Roy, T.S.; Akter, S.; Fahim, M.R.; Gafur, M.A.; Ferdous, T. Incorporation of Ag-doped ZnO nanorod through graphite hybridization: Effective approach for degradation of ciprofloxacin. *Heliyon* **2023**, e13130.
18. Rafique, S.; Bashir, S.; Akram, R.; Jawaid, S.; Bashir, M.; Aftab, A.; Attique, A.; Awan, S.U. In vitro anticancer activity and comparative green synthesis of ZnO/Ag nanoparticles by moringa oleifera, mentha piperita, and citrus lemon. *Ceramics International* **2023**, *49*, 5613-5620.
19. Narayanan, K.B.; Choi, S.M.; Han, S.S. Biofabrication of Lysinibacillus sphaericus-reduced graphene oxide in three-dimensional polyacrylamide/carbon nanocomposite hydrogels for skin tissue engineering. *Colloids and Surfaces B: Biointerfaces* **2019**, *181*, 539-548.
20. Narayanan, K.B.; Park, G.T.; Han, S.S. Antibacterial properties of starch-reduced graphene oxide–polyiodide nanocomposite. *Food Chemistry* **2021**, *342*, 128385.
21. Singh, A.; Singh, N.á.; Afzal, S.; Singh, T.; Hussain, I. Zinc oxide nanoparticles: a review of their biological synthesis, antimicrobial activity, uptake, translocation and biotransformation in plants. *Journal of materials science* **2018**, *53*, 185-201.
22. Jain, D.; Shivani; Bhojiya, A.A.; Singh, H.; Daima, H.K.; Singh, M.; Mohanty, S.R.; Stephen, B.J.; Singh, A. Microbial fabrication of zinc oxide nanoparticles and evaluation of their antimicrobial and photocatalytic properties. *Frontiers in chemistry* **2020**, *8*, 778.
23. Davaeifar, S.; Modarresi, M.-H.; Mohammadi, M.; Hashemi, E.; Shafiei, M.; Maleki, H.; Vali, H.; Zahiri, H.S.; Noghabi, K.A. Synthesizing, characterizing, and toxicity evaluating of Phycocyanin-ZnO nanorod composites: a back to nature approaches. *Colloids and Surfaces B: Biointerfaces* **2019**, *175*, 221-230.
24. Singh, B.N.; Rawat, A.K.S.; Khan, W.; Naqvi, A.H.; Singh, B.R. Biosynthesis of stable antioxidant ZnO nanoparticles by Pseudomonas aeruginosa rhamnolipids. *PLoS One* **2014**, *9*, e106937.
25. Kyomuhimbo, H.D.; Michira, I.N.; Mwaura, F.B.; Derese, S.; Feleni, U.; Iwuoha, E.I. Silver–zinc oxide nanocomposite antiseptic from the extract of bidens pilosa. *SN Applied Sciences* **2019**, *1*, 1-17.
26. Mousavi-Kouhi, S.M.; Beyk-Khormizi, A.; Amiri, M.S.; Mashreghi, M.; Yazdi, M.E.T. Silver-zinc oxide nanocomposite: From synthesis to antimicrobial and anticancer properties. *Ceramics International* **2021**, *47*, 21490-21497.
27. Mahmudin, L.; Suharyadi, E.; Utomo, A.B.S.; Abraha, K. Influence of stabilizing agent and synthesis temperature on the optical properties of silver nanoparticles as active materials in surface plasmon resonance (SPR) biosensor. In Proceedings of the AIP Conference Proceedings, 2016; p. 020041.
28. Jobe, M.C.; Mthiyane, D.M.; Mwanza, M.; Onwudiwe, D.C. Biosynthesis of zinc oxide and silver/zinc oxide nanoparticles from Urginea epigea for antibacterial and antioxidant applications. *Heliyon* **2022**, *8*, e12243.
29. Fouladi-Fard, R.; Aali, R.; Mohammadi-Aghdam, S.; Mortazavi-derazkola, S. The surface modification of spherical ZnO with Ag nanoparticles: A novel agent, biogenic synthesis, catalytic and antibacterial activities. *Arabian Journal of Chemistry* **2022**, *15*, 103658.
30. Makuła, P.; Pacia, M.; Macyk, W. How to correctly determine the band gap energy of modified semiconductor photocatalysts based on UV–Vis spectra. **2018**, *9*, 6814-6817.
31. Xu, J.-J.; Lu, Y.-N.; Tao, F.-F.; Liang, P.-F.; Zhang, P.-A. ZnO Nanoparticles Modified by Carbon Quantum Dots for the Photocatalytic Removal of Synthetic Pigment Pollutants. *ACS omega* **2023**, *8*, 7845-7857.
32. Al-Ariki, S.; Yahya, N.A.; Al-A'nsi, S.a.A.; Jumali, M.H.; Jannah, A.; Abd-Shukor, R. Synthesis and comparative study on the structural and optical properties of ZnO doped with Ni and Ag nanopowders fabricated by sol gel technique. *Scientific Reports* **2021**, *11*, 11948.

33. Ren, T.; Baker, H.R.; Poduska, K.M. Optical absorption edge shifts in electrodeposited ZnO thin films. *Thin Solid Films* **2007**, *515*, 7976-7983, doi:https://doi.org/10.1016/j.tsf.2007.03.185.
34. Saboor, A.; Shah, S.M.; Hussain, H. Band gap tuning and applications of ZnO nanorods in hybrid solar cell: Ag-doped verses Nd-doped ZnO nanorods. *Materials Science in Semiconductor Processing* **2019**, *93*, 215-225.
35. Dasari, M.P.; Godavarti, U.; Mote, V. Structural, morphological, magnetic and electrical properties of Ni-doped ZnO nanoparticles synthesized by co-precipitation method. *Processing and Application of Ceramics* **2018**, *12*, 100-110.
36. Elhamdi, I.; Souissi, H.; Taktak, O.; Elghoul, J.; Kammoun, S.; Dhahri, E.; Costa, B.F. Experimental and modeling study of ZnO: Ni nanoparticles for near-infrared light emitting diodes. *RSC advances* **2022**, *12*, 13074-13086.
37. Bonifácio, M.A.R.; Lira, H.d.L.; Neiva, L.S.; Kiminami, R.H.; Gama, L. Nanoparticles of ZnO doped with Mn: Structural and morphological characteristics. *Materials Research* **2017**, *20*, 1044-1049.
38. Sajjad, M.; Ullah, I.; Khan, M.; Khan, J.; Khan, M.Y.; Qureshi, M.T. Structural and optical properties of pure and copper doped zinc oxide nanoparticles. *Results in Physics* **2018**, *9*, 1301-1309.
39. Riza, M.A.; Go, Y.I.; Harun, S.W.; Anas, S.B.A. Effect of additive concentration on crystalline surface of ZnO nanostructures morphology for enhanced humidity sensing. *Sensors International* **2023**, *4*, 100211.
40. Ismail, A.; Menazea, A.; Kabary, H.A.; El-Sherbiny, A.; Samy, A. The influence of calcination temperature on structural and antimicrobial characteristics of zinc oxide nanoparticles synthesized by Sol–Gel method. *Journal of Molecular Structure* **2019**, *1196*, 332-337.
41. Blount, P.; Marder, L.; Oyegoke, J.; Trad, T. The effects of copper doping on morphology and room-temperature photoluminescence of ZnO nanocolumns. *RSC advances* **2022**, *12*, 32667-32672.
42. Kothe, L.; Albert, M.; Meier, C.; Wagner, T.; Tiemann, M. Stimulation and Enhancement of Near-Band-Edge Emission in Zinc Oxide by Distributed Bragg Reflectors. *Advanced Materials Interfaces* **2022**, *9*, 2102357.
43. Gupta, J.; Mohapatra, J.; Bahadur, D. Visible light driven mesoporous Ag-embedded ZnO nanocomposites: reactive oxygen species enhanced photocatalysis, bacterial inhibition and photodynamic therapy. *Dalton Transactions* **2017**, *46*, 685-696.
44. Vanheusden, K.; Warren, W.; Seager, C.; Tallant, D.; Voigt, J.; Gnade, B. Mechanisms behind green photoluminescence in ZnO phosphor powders. *Journal of Applied Physics* **1996**, *79*, 7983-7990.
45. Zheng, Y.; Chen, C.; Zhan, Y.; Lin, X.; Zheng, Q.; Wei, K.; Zhu, J. Photocatalytic activity of Ag/ZnO heterostructure nanocatalyst: correlation between structure and property. *The Journal of Physical Chemistry C* **2008**, *112*, 10773-10777.
46. Alharthi, F.A.; Alghamdi, A.A.; Al-Zaqri, N.; Alanazi, H.S.; Alsyahi, A.A.; Marghany, A.E.; Ahmad, N. Facile one-pot green synthesis of Ag–ZnO Nanocomposites using potato peeland their Ag concentration dependent photocatalytic properties. *Scientific Reports* **2020**, *10*, 20229.
47. Essawy, A.A. Silver imprinted zinc oxide nanoparticles: Green synthetic approach, characterization and efficient sunlight-induced photocatalytic water detoxification. *Journal of Cleaner Production* **2018**, *183*, 1011-1020.
48. Kumar, A.; Sharma, G.; Naushad, M.; Singh, P.; Kalia, S. Polyacrylamide/Ni0. 02Zn0. 98O nanocomposite with high solar light photocatalytic activity and efficient adsorption capacity for toxic dye removal. *Industrial & Engineering Chemistry Research* **2014**, *53*, 15549-15560.
49. Ha, L.P.P.; Vinh, T.H.T.; Thuy, N.T.B.; Thi, C.M.; Viet, P.V. Visible-light-driven photocatalysis of anisotropic silver nanoparticles decorated on ZnO nanorods: Synthesis and characterizations. *Journal of Environmental Chemical Engineering* **2021**, *9*, 105103, doi:https://doi.org/10.1016/j.jece.2021.105103.
50. Zhang, C.; Kong, C.; Tratnyek, P.G.; Qin, C. Generation of reactive oxygen species and degradation of pollutants in the Fe2+/O2/tripolyphosphate system: Regulated by the concentration ratio of Fe2+ and tripolyphosphate. *Environmental Science & Technology* **2022**, *56*, 4367-4376.
51. Khorrami, S.; Zarrabi, A.; Khaleghi, M.; Danaei, M.; Mozafari, M. Selective cytotoxicity of green synthesized silver nanoparticles against the MCF-7 tumor cell line and their enhanced antioxidant and antimicrobial properties. *International journal of nanomedicine* **2018**, *13*, 8013.
52. Rohde, M.M.; Snyder, C.M.; Sloop, J.; Solst, S.R.; Donati, G.L.; Spitz, D.R.; Furdui, C.M.; Singh, R. The mechanism of cell death induced by silver nanoparticles is distinct from silver cations. *Particle and Fibre Toxicology* **2021**, *18*, 1-24.
53. Hussain, A.; Oves, M.; Alajmi, M.F.; Hussain, I.; Amir, S.; Ahmed, J.; Rehman, M.T.; El-Seedi, H.R.; Ali, I. Biogenesis of ZnO nanoparticles using Pandanus odorifer leaf extract: anticancer and antimicrobial activities. *RSC advances* **2019**, *9*, 15357-15369.
54. Chandrasekaran, S.; Anusuya, S.; Anbazhagan, V. Anticancer, anti-diabetic, antimicrobial activity of zinc oxide nanoparticles: A comparative analysis. *Journal of Molecular Structure* **2022**, *1263*, 133139.
55. Tanino, R.; Amano, Y.; Tong, X.; Sun, R.; Tsubata, Y.; Harada, M.; Fujita, Y.; Isobe, T. Anticancer activity of ZnO nanoparticles against human small-cell lung cancer in an orthotopic mouse ModelZnO nanoparticles inhibit growth of small-cell lung cancer. *Molecular cancer therapeutics* **2020**, *19*, 502-512.

56. González, S.E.; Bolaina-Lorenzo, E.; Pérez-Trujillo, J.; Puente-Urbina, B.; Rodríguez-Fernández, O.; Fonseca-García, A.; Betancourt-Galindo, R. Antibacterial and anticancer activity of ZnO with different morphologies: a comparative study. *3 Biotech* **2021**, *11*, 1-12.
57. Wang, H.; Xing, Z.; Sun, Y.; Jing, Y.; Zhang, J.; Li, X.; Zhang, H.; Shakoor, A.; Guo, J. UV-irradiating synthesis of cyclodextrin–silver nanocluster decorated TiO2 nanoparticles for photocatalytic enhanced anticancer effect on HeLa cancer cells. *Frontiers in Chemistry* **2022**, *10*.
58. Tenjin, T.; Yoshino, N.; Tanaka, S. Evaluation of cell viability by double-staining fluorescence assay. *Gan to Kagaku ryoho. Cancer & Chemotherapy* **2002**, *29*, 2025-2029.
59. Álvarez-Chimal, R.; García-Pérez, V.I.; Álvarez-Pérez, M.A.; Tavera-Hernández, R.; Reyes-Carmona, L.; Martínez-Hernández, M.; Arenas-Alatorre, J.Á. Influence of the particle size on the antibacterial activity of green synthesized zinc oxide nanoparticles using Dysphania ambrosioides extract, supported by molecular docking analysis. *Arabian Journal of Chemistry* **2022**, *15*, 103804.
60. Menichetti, A.; Mavridi-Printezi, A.; Mordini, D.; Montalti, M. Effect of Size, Shape and Surface Functionalization on the Antibacterial Activity of Silver Nanoparticles. *Journal of Functional Biomaterials* **2023**, *14*, 244.
61. Singh, R.; Cheng, S.; Singh, S. Oxidative stress-mediated genotoxic effect of zinc oxide nanoparticles on Deinococcus radiodurans. *3 Biotech* **2020**, *10*, 1-13.
62. Yu, Z.; Li, Q.; Wang, J.; Yu, Y.; Wang, Y.; Zhou, Q.; Li, P. Reactive oxygen species-related nanoparticle toxicity in the biomedical field. *Nanoscale research letters* **2020**, *15*, 1-14.